

Multi-frequency VLBA Polarimetry of the high-redshift GPS Quasar OQ172

Yi Liu^{1,3*}, D. R. Jiang^{2,3}, Minfeng Gu², L. I. Gurvits^{4,5}

¹ Purple Mountain Observatory, Chinese Academy of Sciences, Nanjing 210008, China

² Key Laboratory for Research in Galaxies and Cosmology, Shanghai Astronomical Observatory, Chinese Academy of Sciences, 80 Nandan Road, Shanghai 200030, China

³ Key Laboratory of Radio Astronomy, Chinese Academy of Sciences

⁴ Joint Institute for VLBI ERIC, P.O. Box 2, 7990 AA Dwingeloo, The Netherlands

⁵ Department of Astrodynamics and Space Missions, Delft University of Technology, Kluyverweg 1, 2629 HS Delft, The Netherlands

23 July 2018

ABSTRACT

Multi-frequency Very Long Baseline Array (VLBA) polarimetry observation of the GHz-Peaked Spectrum (GPS) quasar OQ172 (J1445+0958) has been performed at 1.6, 2.2, 4.8, 8.3 and 15.3 GHz in 2005. Core-jet structures are detected in all bands with the jet strongly bent at about 3 mas from the core. The radio emission of the source is polarised at all five bands. We study the Faraday Rotation in the core and jet components at all five bands, and find good linear fits of Faraday Rotation in the core and jet components at 4.8 and 8.3 GHz. At these two frequencies, the Rotation Measure (RM) is ~ 2000 rad m^{-2} in the core and ~ 700 rad m^{-2} in the inner jet components and continues to decrease at the outer jet parts. We find that the depolarisation at 4.8 and 8.3 GHz might be caused by the internal medium in the source. We investigate consistency of the turnover spectra of VLBI components with the Synchrotron Self-Absorption (SSA) and Free-Free Absorption (FFA) models. Although these two models can not be easily distinguished due to the lack of low-frequency data, the physical parameters can be constrained for each model. We find that the large width of the [OIII]₅₀₀₇ line is likely caused by a jet interaction with a Narrow Line Region (NLR) medium. The jet bending, significant RM variations, Faraday depolarisation, spectral turnover, and broad line width of [OIII]₅₀₀₇ could be closely related, likely caused by the same nucleus medium, presumably NLR.

Key words: galaxies: jet – galaxies: nuclei – quasars: individual: OQ172

1 INTRODUCTION

GHz-Peaked Spectrum (GPS) radio sources are characterised by their compact size ($L < \sim 100$ pc) and convex spectra peaked at ~ 0.5 -10 GHz received frequencies (O’Dea et al. 1991). GPS radio galaxies often have a compact symmetric structure on the scale of milli- to centi-arcseconds, while GPS quasars appear with a typical core-jet morphology, in line with the Active Galactic Nucleus (AGN) unified schemes. Like most GPS sources, the quasar OQ172 (J1445+0958) at $z = 3.552$, shows no kpc-scale radio structure. VLBI images have revealed a compact N-S elongation at 18 cm (Dallacasa et al. 1995) and 6 cm (Fomalont et al. 2000), also detected with the Space VLBI VSOP at 6 cm (Gurvits 2003). Two more distant compact southern com-

ponents were detected at 13 and 4 cm (Fey & Charlot 2000). The known so far centi-arcseconds structural pattern resembles a ‘clockwise semicircle’ with the core in the northernmost position.

At the peak ‘turnover’ frequency of GPS sources, ν_T , optically thin radio synchrotron radiation (for $\nu > \nu_T$) transits to optically thick emission (for $\nu < \nu_T$), though there is still a debate over whether this is caused by Synchrotron Self-Absorption (SSA) or Free-Free Absorption (FFA) (O’Dea 1998). O’Dea & Baum (1997) and Snellen et al. (2000) suggested that the observed anti-correlation between ν_T and the linear size of GPS sources could be explained by SSA. However, Bicknell et al. (1997) proposed an alternative model with FFA occurring in an ionized gas surrounding the radio emitting regions. To discriminate between these two models, multi-frequency VLBI studies are required.

* E-mail: liuyi@pmo.ac.cn

OQ172 has an extremely high rest-frame rotation measure ($RM > 20,000 \text{ rad m}^{-2}$; Udomprasert et al. 1997), one of the highest among ~ 20 known high-RM sources. At only 10 mas ($R_{proj} \sim 90 \text{ pc}$) from the VLBI core, the RM falls to $< 100 \text{ rad m}^{-2}$. Such a steep RM gradient might cause intrinsic depolarisation of the synchrotron emission in the VLBI core regions. The former could be caused by weakening of the regular magnetic field and/or increasing density of the ionised gas.

As a further evidence of unusual properties of the physical environment in the core of OQ172, the near infrared (NIR) spectrum shows a typical $H\beta$ broad emission line of Full Width at Half Maximum (FWHM) of $\sim 3,700 \text{ km s}^{-1}$, but an unusually large width of $2,200 \text{ km s}^{-1}$ for the narrow $[\text{OIII}]_{5007}$ line (Hirst et al. 2003). Mantovani et al. (1998) relate the width of the $[\text{OIII}]_{5007}$ line to the interaction of the strongly bent VLBI jet with the NLR medium.

We performed a 10-hour-long multi-frequency VLBA polarimetry observation at 1.6, 2.2, 4.8, 8.3 and 15.3 GHz aiming to investigate the unusual physical circumnuclear environment of the GPS quasar OQ172 by studying: (1) the distribution of polarised emission and rotation measure, (2) the GPS absorption mechanism and associated opacity, and (3) variations of physical parameters along the jet. Specifically, we aimed to estimate parameters of the circumnuclear environment of OQ172 on the basis of the observed properties at the redshifted rest-frame frequencies within the range 6-70 GHz.

The Hubble constant $H_0 = 70 \text{ km s}^{-1} \text{ Mpc}^{-1}$, $\Omega_M = 0.3$ and $\Omega_\Lambda = 0.7$ are used throughout this paper. With these cosmological parameters, at the redshift of OQ172, 1 mas corresponds to 8.84 pc. The paper is organised as follows. In Sect. 2 the observation and data reduction are described. The results and discussions are presented in Sect. 3, followed by our conclusions in Sect. 4.

2 OBSERVATION AND DATA REDUCTION

Our multi-frequency polarimetric continuum observation of OQ172 was conducted at 1.6, 2.2, 4.8, 8.3, and 15.3 GHz on 2005 June 22 with the VLBA for the total duration of about 10 hours. The left- and right-circular polarisation (LCP and RCP, respectively) signals were recorded in 8 baseband channels (BBCs) with a total bandwidth of 128 MHz and 2-bit sampling. BBCs were placed in close pairs to avoid Faraday depolarisation across each pair for an assumed rest-frame $RM < 50,000 \text{ rad m}^{-2}$. In each frequency band, the BBCs were separated as widely as possible in order to achieve the most accurate estimate of the rotation measure. The theoretical RMS noise in total intensity images with integration time of 20 mins at 1.6, 2.2, 4.8 GHz, 90 mins at 8.3 GHz and 160 mins at 15.3 GHz do not exceed $0.15 \text{ mJy beam}^{-1}$. However, the real RMS noise measured at each band is usually higher than the theoretical value, which is shown in Figure 2. In each of the 5 frequency bands, we observed the primary flux density calibrator 3C286 in 2 scans (4 min each), the instrumental polarisation (D -term) calibrator OQ208 over PA range $> 100^\circ$ in 5 scans (6 min each). Three scans were used for each of two electric vector position angle (EVPA) calibrators, 3C279 (3 min each) and

3C345 (4 min each). Table 1 lists the details of the observation.

The recorded data were first processed at the VLBA correlator in Socorro (New Mexico, USA) and then calibrated and fringe-fitted using the NRAO Astronomical Image Processing System (AIPS) software, as described by Zavala & Taylor (2004). Self-calibration and imaging were with the Difmap program (Shepherd, Pearson, & Taylor 1994). The estimated uncertainty of the amplitude calibration in self-calibration process is about $5 \sim 10$ percent, these values are consistent with typical amplitude corrections reported by Homan et al. 2002. In the course of the data reduction, each of four different IF channels at each of the five observing bands was processed separately. In all steps of the data processing, we used the VLBA Los Alamos as the reference antenna. We used the non-polarised compact source OQ208 to calibrate the instrumental polarisation of the antennas by using the AIPS task LPCAL. To ensure that the D -term solutions were physically meaningful, we checked the distribution of the normalized RL/RR visibility in complex (real and imaginary) plane, with and without instrumental calibration. We found that the RL/RR visibility appeared well clustered after the instrumental calibration (see <http://www.vla.nrao.edu/astro/calib/polar/>). The solution shows that the instrumental polarisations are typically about 1% at 1.6, 2.2, 4.8 GHz and about 1.5% for 8.3 and 15.3 GHz.

Since EVPA calibrators recommended by NRAO are all stable across bandwidth (see <http://www.vla.nrao.edu/astro/calib/polar/>), we calibrated EVPA at each baseband by comparing to the calibrator at a close arbitrary frequency assuming small rotation across base-bands. Since the source 3C286 is a stable EVPA calibrator with its R/L phase difference of 66° (see <http://www.vla.nrao.edu/astro/calib/polar/>), we used this source to correct the EVPA of the target source at 1.6, 2.2, and 4.8 GHz. The absolute EVPA calibration at 8.3 GHz was performed by using an integral EVPA of 3C279 within 6 days (observed on 2005 Jun 17) of our observation from the NRAO VLA/VLBA Polarisation Calibration Database, in which the R/L phase difference was given as $-142.2 \pm 1.8^\circ$. However, 3C279 has no available absolute EVPA at 15.3 GHz, thus the true EVPA at this frequency was estimated by using RM of -79 rad m^{-2} obtained at the two lower frequencies of 4.8 and 8.3 GHz (Chen, Shen & Feng 2010). This led us to the estimate of the R/L phase difference for 3C279 at 15.3 GHz of $112.5 \pm 1.7^\circ$.

3 RESULTS AND DISCUSSION

3.1 The Radio Structure

Since the steep-spectrum structures fade away rapidly with increased frequencies, the size of detected radio emission in an intensity distribution image decreases rapidly with increased frequencies. This physical effect is further amplified by typically lower sensitivities of VLBI systems at higher frequencies. The total intensity images of OQ172 observed at five frequencies have been presented as preliminary results in our previous paper (Liu et al. 2016). In this paper, we update the images (Figure 1) by adding the model-fit on

Table 1. VLBA observational parameters

Sources (1)	IF Frequencies (GHz) (2)	BandWidth(MHz) (3)	Scan (4)	Total on-source integration (min) (5)
OQ172, OQ208, 3C286	1.412, 1.502, 1.592, 1.683	8	24	72
OQ172, OQ208, 3C286	2.166, 2.211, 2.256, 2.302	8	24	72
OQ172, OQ208, 3C286	4.630, 4.770, 4.910, 5.051	8	24	102
OQ172, OQ208, 3C279	8.116, 8.196, 8.396, 8.537	8	23	134
OQ172, OQ208, 3C279	15.140, 15.220, 15.421, 15.561	8	34	191

individual components (core and jet, see below). The figure clearly demonstrates a consistent core-jet morphology at all five bands (see also Liu et al. 2016). A combination of all five images offers an opportunity to trace the jet in details. Our 1.6 and 4.8 GHz images are consistent with those by Udomprasert et al (1997). At 2.2 GHz, the source has a very similar structure to that at 1.6 GHz, albeit more resolved in outer jet regions. At 8.3 and 15.3 GHz, the images show jet bending at ~ 3 mas from the core. At the higher frequencies of 8.3 and 15.3 GHz and correspondingly higher angular resolution, the jet knots are fragmented into smaller size features. A combination of our images at five frequency shows the overall jet structure as pointed toward the west from the core, followed by a sharp bend toward south at about 3 mas and yet another bend toward east at about 20 mas.

After obtaining the source’s images, we performed model-fitting on the self-calibrated visibility data with circular Gaussian components. We assumed the brightest component in each image to be stationary and used it as a reference point. The coordinates of other components were measured relative to it. Figure 1 shows the naturally weighted images with model-fitted circular Gaussian components at each band. Parameters of the fitted components and the derived brightness temperature (T_B) in the source frame for both components are listed in Table 2. The source-frame T_B is estimated by using the following expression (Ghisellini et al. 1993),

$$T_B = 1.77 \times 10^{12} \left(\frac{f_\nu}{\text{Jy}}\right) \left(\frac{\nu}{\text{GHz}}\right)^{-2} \left(\frac{\theta_d}{\text{mas}}\right)^{-2} (1+z), \quad (1)$$

where f_ν is flux density at frequency ν , and θ_d is the component angular size.

3.2 The Polarisation Properties and Rotation Measure

In Figure 2, we show the integrated polarisation images, which include all baseband channels at each frequency. We found that the polarisation images at a single baseband are similar to the integrated ones at all five bands. This implies that the bandwidth depolarisation is generally not significant. The polarisation structures of OQ172 are detected in all five frequency bands. The region with a detectable linear polarisation decreases gradually in size from 20 mas to a few mas with increasing observational frequencies due to increasing resolution and lower surface brightness. Compared to ‘normal’ AGNs with typical radio polarisation at the level of several percents, GPS sources are generally less polarised (O’Dea 1998; Stanghellini et al. 1998). The overall fractional polarisation from low to high frequencies in our observation is 0.39%, 0.46%, 1.60%, 1.38% and 0.6% in five frequency

bands, respectively. The fractional polarisation is higher in the jet components than that in the core, as clearly visible in Figure 2. The relatively low polarisation level in the core region is typical for radio-loud AGNs and might be due to the inner regions effects of high opacity, high depolarisation, complex morphology and plasma effects in the immediate vicinity of AGN (e.g. Taylor 1998; Homan et al. 2009; Chen et al. 2010). The depolarisation effect across the 8 MHz sub-band is generally small at all five frequencies, however, the relatively low fractional polarisation at two low frequencies (1.6 and 2.2 GHz) could still be partly caused by the depolarisation from the Faraday rotation, which is expected to be higher within the same width of a sub-band compared to the higher frequencies. A lower resolution at a lower frequency adds up to this effect (Chen et al. 2010; 2011).

The polarisation structure at 4.8, 8.3 and 15.3 GHz can be traced with higher degree of detail than at lower frequencies of 1.6 and 2.2 GHz due to an in-beam depolarisation at a lower angular resolution. Comparing to the earlier 5 GHz polarisation image presented by Udomprasert et al. (1997), we found that the polarisation level in the core region is lower although the two observations provided the similar total flux density. In order to search for possible variability in polarised structures in OQ172, we have re-processed the Udomprasert’s data from the NRAO archive, using the same processing approach as for our own data. In order to evaluate a potential effect of bandwidth depolarisation, we compared the polarised images at each sub-band by Udomprasert’s (1997) with those from our data. We find that the fractional polarisation in the core component at each sub-band is all lower than that in Udomprasert et al. (1997). This, together with the similar setting of segregated sub-bands in Udomprasert’s data and ours, indicates strongly that the lower fractional polarised flux density in the core component in our 4.8 GHz data is unlikely due to the bandwidth depolarisation effect. We also reduced another VLBA archive data set from the epoch 2000.6 at 5 GHz. Figure 3 shows the distributions of visibility amplitudes of OQ172 at these three epoches. We found an obvious change of visibility amplitudes at long baselines. The visibility amplitude was almost 20 times at the second epoch 2000.6 at the uv radius longer than $90 \times 10^6 \lambda$. The visibility amplitudes remained high at the longest baselines in the third available observing epoch 2005.6 too. While the new component was not found close to the core in our and previous 5 GHz observations, a new component can be clearly identified in our 15.3 GHz image (component U7, see Figure 1). This suggests that there would have been a new component when the visibility amplitude changes but it needs higher resolution to distinguish. The new component might manifest itself in both the source’s flux density and polarisation properties. This new component does not increase the total flux den-

sity, therefore, it could be a newly-seen but not new-born component in the innermost core region, moving outwards relative to the core. It might affect the polarisation flux and lead to a variation of the distribution of the polarised emission at 4.8 GHz.

The linear polarisation can be estimated for each component by using the total intensity and the Stokes Q and U flux densities from the model fitting. The corresponding linearly polarised flux density and positional angle were obtained as $P = (Q^2 + U^2)^{1/2}$ and $\chi = 1/2 \arctan(U/Q)$, respectively. The fractional polarisation m is calculated as $m = P/I$. The uncertainties of P , χ and m were derived using a method suggested by Hovatta et al. (2012), which includes the D -term leakage effect. The estimates of P , χ , and m are listed in Table 3 for each component in four IFs at all five frequencies, as well as their uncertainties.

The rotation of the polarisation plane in the magnetised medium is given by the following formula (e.g. Spitzer 1978; Taylor 1998):

$$RM = 812 \int_0^L n_e B_{\parallel} dl \quad \text{rad m}^{-2}, \quad (2)$$

where RM is the Rotation Measure in rad m^{-2} , n_e is the electron number density in cm^{-3} , B_{\parallel} is magnetic field in mG, l is the length in pc along the line of sight from the observer, and L is the path length in pc. As expected, we found that the polarisation angles χ were different at different frequencies. There are significant variations in polarisation angles even in adjacent IF channels within the same frequency band, while the variations in polarised flux densities are less pronounced.

In order to examine whether the variation of polarisation angles (χ) is associated with Faraday Rotation, we attempted to obtain linear fits over the entire wavelength range at each frequency band allowing for $n\pi$ ambiguities in the polarisation position angles with their uncertainties. Figures 4 - 6 present the ' $\chi - \lambda^2$ ' relation for core (in Figure 4) and jet components (1.6 and 2.2 GHz in Figure 5 and 4.8, 8.3, and 15.3 GHz in Figure 6) at all five frequencies. The RM measurements of the core and two innermost jet components at 4.8 and 8.3 GHz were presented as a preliminary results in our previous paper (Liu et al. 2013). In this work, we reproduce those figures in order to make systematic study by combining with other bands, and by extending it to all jet components. At two lower frequencies (1.6 and 2.2 GHz), both the direct measurements (in each middle panel) of polarisation position angles and those with $n\pi$ rotational ambiguities are displayed for the core component in Figure 4(a) and 4(b). While there is no good linear fit on the directly measured polarisation position angles, the rotation measure $\sim 2000 \text{ rad m}^{-2}$ could be obtained at both frequencies from the linear fit by adding minimal $n\pi$ rotational ambiguities. However, we find that a similar RM can always be obtained by adding same rotational ambiguities for any given polarisation angles at four IFs. Therefore, the RM of core component estimated from adding rotational ambiguities at 1.6 and 2.2 GHz is not reliable. In contrast, a good linear fit without adding any rotational ambiguities can be found for the core component at 4.8 and 8.3 GHz, which are plotted in Figure 4(c) and 4(d). At 4.8 GHz, the RM value of the core component, $2089 \pm 225 \text{ rad m}^{-2}$, is very

similar to that at 8.3 GHz, $2028 \pm 172 \text{ rad m}^{-2}$. At 15.3 GHz, the ' $\chi - \lambda^2$ ' relation is apparently non-linear, which likely implies a contribution from rotation within the core itself. By adding $n\pi$ rotational ambiguities, a RM value of $2.911 \times 10^5 \pm 1082 \text{ rad m}^{-2}$ is found, more than two orders of magnitude higher than those at 4.8 and 8.3 GHz. Such an extremely high value, and the inconsistency with other bands, indicate that the value should be treated with caution.

In Figures 5 and 6, the ' $\chi - \lambda^2$ ' relations for each jet component at all five frequencies are presented, in which only the directly measured polarisation position angles in each single baseband are plotted. In most cases, there are no significant linear relation in jet components at 1.6 (Figure 5(a)-(e)) and 2.2 GHz (Figure 5(f)-(j)). However, the variation of χ tends to decrease along the jet, likely indicating a smaller RM towards outer jet regions. At 4.8 GHz (Figure 6(a)-(f)) and 8.3 GHz (Figure 6(g)-(l)), except for C3 and X3, all jet components show a good linear fits on the ' $\chi - \lambda^2$ ' relation, and the resulting RM values of the corresponding jet components are generally consistent within the errors at two bands. The innermost jet component C6 and X6 show a comparable RM, $1972 \pm 207 \text{ rad m}^{-2}$ and $2102 \pm 124 \text{ rad m}^{-2}$, respectively. However, the RM values drop to $722 \pm 132 \text{ rad m}^{-2}$ in C5 and $780 \pm 105 \text{ rad m}^{-2}$ in X5 at a distance of $\sim 3 \text{ mas}$ from the core. Along the jet, the RM values show a similar tendency of monotonic decrease at 4.8 and 8.3 GHz, from $455 \pm 96 \text{ rad m}^{-2}$ in C4 to $113 \pm 36 \text{ rad m}^{-2}$ in C1, and $470 \pm 127 \text{ rad m}^{-2}$ in X4 to $176 \pm 138 \text{ rad m}^{-2}$ in X1. Our results at 4.8 GHz are consistent with that in Udomprasert et al (1997). The RM can be obtained even in the outer jet components at 4.8 and 8.3 GHz, i.e., C1 and X1, suggesting that the Faraday screen extends to much larger radii in this source. Besides consistency check, we also tried to connect the RM values at 4.8 and 8.3 GHz, and found that the core and inner three jet components (C6/X6, C5/X5 and C4/X4) are consistent with appropriately adjusted rotational ambiguities, but the three outer jet components are not. This indicates that the medium responsible for Faraday rotation in the core and inner jet regions is different from that in the outer jet. At 15.3 GHz (Figure 6(m)-(q)), it appears that all the ' $\chi - \lambda^2$ ' relations based on the directly measured polarisation angles are non-linear, thus reliable estimates of RM cannot be obtained. At low frequencies (1.6 and 2.2 GHz), the rotational ambiguities might be the main issue when obtaining a RM value from a linear fit. However, at 15.3 GHz, the rotational ambiguities are less of a problem. The observed non-linear ' $\chi - \lambda^2$ ' relation may be caused by the low signal to noise ratio of the polarisation flux detection since the corresponding uncertainties for polarisation position angles are relatively larger. Quantitatively, a RM value of 2500 rad m^{-2} corresponds to a polarisation angle variation of about 0.053 rad (i.e., $\sim 3^\circ$) in observing band of $0.21 \times 10^{-4} \text{ m}^2$ at 15.3 GHz. It therefore requires a very high precision in polarisation angle measurements. The situation is even worse for a lower RM value. A broader bandwidth is needed to the observed RM properties can measure the RM reliably in these cases. Alternatively, the observed RM properties can be related to the properties of the jet itself, such as an internal rotation within the jet.

Table 3 shows the depolarisation in the core and jet

Table 2. Component parameters in OQ172.

Frequency (GHz) (1)	Component (2)	Flux Density (Jy) (3)	Radius from Core (mas) (4)	Position Angle (deg) (5)	Size (mas) (6)	Brightness Temperature (10^{10} K) (7)
1.6 GHz	Core	0.766±0.074	0.00	...	1.93	69.78
	L5	0.492±0.064	3.38± 0.04	-148	1.60	63.56
	L4	0.381±0.053	11.06± 0.09	-174	2.37	22.43
	L3	0.174±0.041	14.58± 0.10	-178	2.29	10.97
	L2	0.054±0.020	21.71± 0.74	-199	4.85	0.76
	L1	0.054±0.020	24.34± 0.43	-215	3.10	1.86
2.2 GHz	Core	0.859±0.081	0.00	...	2.02	33.12
	S5	0.382±0.058	3.12± 0.05	-140	1.40	31.39
	S4	0.236±0.044	9.12± 0.14	-172	2.50	6.08
	S3	0.207±0.041	14.04± 0.11	-175	1.75	10.89
	S2	0.042±0.025	20.68± 1.65	-196	6.05	0.18
	S1	0.031±0.017	24.65± 0.60	-215	2.70	0.68
4.8 GHz	Core	0.256±0.029	0.00	...	0.30	96.75
	C6	0.234±0.028	1.38± 0.03	-111	0.88	10.28
	C5	0.117±0.020	3.08± 0.03	-106	0.60	11.05
	C4	0.077±0.017	4.32± 0.05	-123	0.87	3.46
	C3	0.054±0.014	6.53± 0.08	-143	1.02	1.77
	C2	0.067±0.019	10.62± 0.45	-165	3.29	0.21
	C1	0.054±0.014	14.91± 0.22	-170	1.96	0.48
8.3 GHz	Core	0.304±0.028	0.00	...	0.31	36.67
	X6	0.124±0.019	1.32± 0.05	-111	0.93	1.66
	X5	0.074±0.014	3.18± 0.07	-109	0.89	1.08
	X4	0.032±0.010	4.76± 0.16	-127	1.24	0.24
	X3	0.019±0.008	6.86± 0.16	-143	0.98	0.23
	X2	0.039±0.025	11.05± 1.27	-164	3.92	0.03
	X1	0.016±0.008	14.72± 0.34	-169	1.49	0.08
15.3 GHz	Core	0.181±0.025	0.00	...	0.30	6.85
	U7	0.036±0.013	.51± 0.02	-142	0.29	1.46
	U6	0.035±0.012	1.47± 0.08	-114	0.58	0.35
	U5	0.024±0.011	3.18± 0.16	-107	0.77	0.14
	U4	0.013±0.010	4.27± 0.42	-123	1.10	0.04
	U3	0.008±0.010	6.70± 0.76	-140	1.20	0.02

Notes: (1): Observing frequency. (2): Component name. (3): Total flux density of each components. (4): Distance of each component from the core. (5): Position angle of each component. (6): Major axis of each component. (7): the bright temperature of each component in units of 10^{10} K.

components between different frequencies. In our observations, the bandwidth depolarisation across the 8 MHz sub-band cannot explain the depolarisation. While interpretation of depolarisation in the core by opacity effects is difficult, the depolarisation of optically thin outer jet components might indicate on internal or external origin of the effect. A number of depolarisation models are reported in the literatures: the Slab model (Burn 1966), Tribble model (Tribble 1991), Rossetti-Mantovani model (Rossetti et al. 2008; Mantovani et al. 2009), and the Repolariser model (Homan et al. 2002; Mantovani et al. 2009; Hovatta et al. 2012). In this work, we investigate whether the depolarisation is caused by an internal or external Faraday screen by studying the depolarisation behavior in the jet components and by using the model described in Hovatta et al. (2012), in which a linearized formula $\ln m = \ln m_0 + b\lambda^4$ is used for fitting the observed fractional polarisation m at the corresponding wavelength λ . This method provides the total depolarisation b from the slope of the fit. Then, the position on the diagram of the fitted b with the observed $|\text{RM}|$, will give us clues on whether the studied depolarisation is caused by internal or external Faraday screen (see details in Figure 7 of Hovatta et al. 2012). Here, we only focused on 4.8 and 8.3 bands, at

which the best RM linear fits were found for most jet components. The linear fits parameters, $\ln m_0$ and slope b together with rotation measure values RM, are listed in Table 4. We find that the jet components with measured RM at 4.8 and 8.3 GHz are all above the solid line in Figure 7 of Hovatta et al. (2012), indicating that the depolarisation behavior in the jet is dominated by an internal Faraday depolarisation at these two frequencies, even in the outer regions of the jet.

The RM associated with the Milky Way is usually not greater than 200 rad m^{-2} at any direction (Pushkarev 2001; Pshirkov et al. 2011; Oppermann et al. 2012). At the direction of OQ172, the approximate value of Galactic RM is less than several tens of rad m^{-2} . Not only is this much smaller than the RM values in the core and inner jet components, but also much smaller than the RM values in the outer jet components. Therefore, the major contribution to the high RM values is associated with the medium outside the Milky Way. Although we cannot rule out that this contribution is provided by the intervening intergalactic medium, we consider as more plausible an assumption that the high RM values are formed in the immediate vicinity of OQ172. OQ172 is one of only 20 sources known for having the highest RM values in excess of 1000 rad m^{-2} . The rest-frame

value of the RM is higher than the observed one by the factor $(1+z)^2$, leading to ~ 40000 rad m $^{-2}$ at the redshift of OQ172. About half of these highest RM sources are Compact Steep Spectrum (CSS) sources (Taylor, Inoue, & Tabara 1992). The GPS sources are even smaller in size than CSS sources, which is commonly explained by their youth and/or confinement by the surrounding medium. Indeed, the extremely high value of RM in the core and inner jet regions of OQ172 is indicative of the presence of dense gas within central ~ 3 mas, corresponding to the projected linear size of about 26.5 pc.

3.3 Physical Model-fitting

In the framework of the relativistic beaming and the standard synchrotron self-Compton (SSC) theory, the physical quantities in the jets can be estimated under the assumption of homogeneous spherically distributed emitting plasma (Ghisellini et al. 1993; Readhead 1994) or an inhomogeneous relativistic jet model (Blandford & Königl 1979 and Königl 1981). In this work, we investigate physical model-fitting under the homogeneous spherical assumption. Single-dish observations (Steppe et al. 1995, Edwards & Tingay 2004) indicate that the turnover frequency of OQ172 as a whole is located around $1 \sim 2$ GHz. The VLBA resolution at lower frequencies of 1.6 and 2.2 GHz is insufficient to distinguish the core and inner jet components as visible at the higher frequencies of 4.8, 8.3 and 15.3 GHz. In order to analyse the radio spectrum for structures with similar sizes, we combine the core and inner jet components into a core region component at 4.8 (core+C6), 8.3 (core+X6) and 15.3 GHz (core+U7+U6) with comparable size with the core at 1.6 and 2.2 GHz. The combined component at 4.8, 8.3 and 15.3 GHz as well as the core component at 1.6 and 2.2 GHz are called hereafter the ‘core region component’, representing the total radio emission within 3 mas. The radio spectrum of this core region component is constructed using its total radio emission at each band, which clearly shows a turnover (see Figure 7). In contrast, there is no turnover in the spectra of other jet components. This strongly indicates that the SSA/FFA absorption occurs in the core region (within 3 mas), not in the outer regions.

Following O’Dea (1998), we apply both SSA and FFA absorption models to fitting the spectrum of the core region component using formulas presented by Kemeno et al. (2000):

$$S_\nu = S_0 \nu^{2.5} [1 - \exp(-\tau_s \nu^{\alpha-2.5})], \quad (3)$$

and

$$S_\nu = S_0 \nu^\alpha \exp(-\tau_f \nu^{-2.1}), \quad (4)$$

where τ_s and τ_f are the SSA and FFA coefficients, S_0 , ν and α are the flux density at 1 GHz, the frequency in GHz, and the spectra index, respectively.

Both SSA and FFA can well fit the spectrum of the core region component (see Figure 7 and Table 4). However, the two models could not be easily distinguished since the peak frequency is close to the lowest frequency of our observation and due to the lack of low-frequency observing data (i.e. at frequencies lower than the turnover frequency). Future observations at lower frequencies would help to resolve this ambiguity. While a specific model of absorption cannot be

determined yet, some conclusions on physical parameters in the core region can be made. Based on the SSA model, we can obtain the equipartition magnetic field $B \sim 3.4 \pm 0.6$ mG from the relationship in O’Dea (1998)

$$\nu_m \sim 8B^{1/5} S_m^{2/5} \theta^{-4/5} (1+z)^{1/5} \text{ GHz}, \quad (5)$$

where the magnetic field is in G, S_m in Jy is a flux density at a peak frequency ν_m , z is the redshift, θ is the angular size in mas at ν_m , which is taken as the core size at 1.6 GHz since the peak frequencies are very close to 1.6 GHz.

Alternatively, in the FFA model, the relationship between the FFA coefficient of τ_f and the emission measure $\int_0^L n_e^2 dl$ can be expressed as (see, e.g., Gallimore, Elitzur & Baum 2006):

$$\tau_f = 0.08235 \nu_f^{-2.1} T_e^{-1.35} \int_0^L n_e^2 dl, \quad (6)$$

where ν_f is the peak frequency in GHz, T_e is the electron temperature in K, the electron density n_e in cm $^{-3}$ and the path-length integral l in pc, and L is the FFA path length. Assuming the equipartition brightness temperature of 5×10^{10} K (Readhead 1994) as intrinsic value of T'_B , our estimates of the brightness temperature (see Table 2) can be used to estimate the Doppler factor with $\delta = T_B/T'_B \sim 10$ (Ghisellini et al. 1993). The viewing angle then can be constrained as $\sin \theta \leq 1/\delta$ (Ghisellini et al. 1993; Urry & Padovani 1995). Assuming $\sin \theta \sim 1/\delta$ and FFA happening in the core region component with size of ~ 3 mas (corresponding to a projected linear size of $l \sim 26.5$ pc), the path-length integral can be constrained as $\int dl = l/\sin \theta \sim 265$ pc along the line of sight. This size is consistent with the NLR size estimated from $R_{NLR} = 295 \times L_{bol,46}^{0.47 \pm 0.13}$ pc (Mor et al. 2009) with the bolometric luminosity $\log L_{bol} = 46.10$ erg s $^{-1}$. The average electron density of the FFA absorber is $n_e \sim 10^3 (T_e/10^4)^{0.675}$ cm $^{-3}$, consistent with typical values in NLR ($n_e \sim 10^3$ cm $^{-3}$, and $T_e \sim 10^4$ K, Peterson 1997). This indicates that FFA is likely caused by the NLR medium. Based on this estimated electron density, and in combination with the relationship between RM, the electron density and parallel magnetic field (Equation 1), we can obtain the magnetic field $B_{\parallel} \sim 2.9$ mG by assuming RM in the core region caused by the same plasma as FFA. In some GPS/CSS sources, such as OQ 208, SSA and FFA might co-exist (e.g., Xie et al. 2005). While our model-fitting does not allow us to distinguish between the two models, we notice that the physical parameters calculated under the assumption of a single absorption model (SSA or FFA) should be treated as constraints, rather than real measurements.

3.4 The Jet-NLR Interaction

Based on the CIV line measurements from the SDSS spectrum, we estimated the black hole mass $M_{BH} = 2.8 \times 10^9 M_\odot$ using the empirical relation by Kong et al. (2006)

$$M_{BH}(CIV) = 4.6 \times 10^5 \left(\frac{LCIV}{10^{42} \text{ erg s}^{-1}} \right)^{0.60 \pm 0.16} \left[\frac{\text{FWHM}_{CIV}}{1000 \text{ km s}^{-1}} \right]^2 M_\odot, \quad (7)$$

The value is consistent within the error (typically, 0.5 dex) for a black hole mass $8 \times 10^9 M_\odot$ estimated from the $H\beta$ line, measured in the IR spectrum by Hirst et al. (2003).

Despite a low spectral resolution and blending with the

Table 3. Parameters of polarised components in OQ172

Freq (GHz) (1)	(2)	Core (3)	L5 (4)	L4 (5)	L3 (6)	L2 (7)	L1 (8)	(9)
1.436	P (mJy)	4.57 ± 1.63	2.84 ± 1.46	4.92 ± 1.41	3.15 ± 1.26	4.57 ± 1.25	6.72 ± 1.25	...
	χ ($^\circ$)	-88.2 ± 10.2	-9.8 ± 14.8	68.1 ± 8.2	32.7 ± 11.4	-21.3 ± 7.8	13.4 ± 5.3	...
	m (%)	0.6 ± 0.2	0.5 ± 0.3	1.3 ± 0.3	2.8 ± 1.3	8.5 ± 3.0	11.3 ± 1.9	...
1.466	P (mJy)	6.17 ± 2.12	1.63 ± 1.97	6.31 ± 1.93	3.79 ± 1.83	5.81 ± 1.83	7.09 ± 1.83	...
	χ ($^\circ$)	-23.4 ± 9.8	-15.5 ± 17.2	77.4 ± 8.8	6.7 ± 13.8	-24.2 ± 9.0	23.2 ± 7.4	...
	m (%)	0.8 ± 0.3	0.3 ± 0.4	1.6 ± 0.4	2.2 ± 1.7	10.8 ± 3.7	13.2 ± 3.2	...
1.636	P (mJy)	4.81 ± 2.05	1.68 ± 1.81	3.87 ± 1.77	4.11 ± 1.70	6.87 ± 1.69	6.49 ± 1.69	...
	χ ($^\circ$)	-51.1 ± 12.2	-50.3 ± 19.5	56.8 ± 14.2	26.8 ± 11.9	-20.1 ± 7.0	40.8 ± 7.4	...
	m (%)	0.6 ± 0.3	0.4 ± 0.4	1.0 ± 0.5	2.4 ± 0.9	12.1 ± 2.9	13.5 ± 3.5	...
1.687	P (mJy)	3.48 ± 2.16	1.93 ± 1.93	3.67 ± 1.90	3.77 ± 1.83	5.74 ± 1.82	6.34 ± 1.82	...
	χ ($^\circ$)	-73.5 ± 17.8	-7.4 ± 17.1	68.9 ± 15.5	44.2 ± 10.9	-14.0 ± 9.0	29.0 ± 8.2	...
	m (%)	0.4 ± 0.3	0.4 ± 0.4	0.4 ± 0.4	2.7 ± 1.1	10.6 ± 2.6	12.8 ± 5.0	...
Freq (GHz) (1)	(2)	Core (3)	S5 (4)	S4 (5)	S3 (6)	S2 (7)	S1 (8)	(9)
2.170	P (mJy)	4.72 ± 2.95	1.77 ± 2.97	8.17 ± 2.92	13.84 ± 2.91	6.13 ± 2.88	3.41 ± 2.88	...
	χ ($^\circ$)	162.7 ± 17.9	-20.7 ± 19.4	111.2 ± 10.2	15.1 ± 6.0	15.4 ± 13.4	90.5 ± 24.1	...
	m (%)	0.5 ± 0.6	0.5 ± 0.5	2.2 ± 0.8	6.7 ± 0.8	13.6 ± 6.3	13.1 ± 11.0	...
2.200	P (mJy)	5.57 ± 2.40	1.17 ± 2.19	7.87 ± 2.14	12.34 ± 2.14	6.25 ± 2.12	3.11 ± 2.12	...
	χ ($^\circ$)	104.8 ± 12.3	-30.5 ± 19.4	81.2 ± 7.7	5.7 ± 4.9	10.5 ± 9.7	85.5 ± 19.4	...
	m (%)	0.6 ± 0.3	0.3 ± 0.5	2.1 ± 0.9	5.9 ± 0.9	14.5 ± 5.2	11.7 ± 6.6	...
2.245	P (mJy)	5.45 ± 2.06	2.65 ± 1.76	7.92 ± 1.71	13.29 ± 1.70	6.69 ± 1.68	3.89 ± 1.68	...
	χ ($^\circ$)	170.2 ± 10.8	-57.0 ± 18.9	95.9 ± 6.1	-35.4 ± 3.6	11.5 ± 7.1	88.9 ± 12.3	...
	m (%)	0.6 ± 0.2	0.7 ± 0.4	2.7 ± 0.7	6.4 ± 0.8	15.9 ± 3.9	12.5 ± 5.4	...
2.306	P (mJy)	3.98 ± 2.71	1.25 ± 2.49	8.38 ± 2.45	12.34 ± 2.45	5.18 ± 2.43	4.78 ± 2.43	...
	χ ($^\circ$)	93.3 ± 19.4	-52.1 ± 17.2	74.0 ± 8.3	-24.7 ± 5.6	10.1 ± 13.4	85.2 ± 14.5	...
	m (%)	0.5 ± 0.3	0.3 ± 0.6	2.8 ± 1.0	6.0 ± 1.1	12.3 ± 5.5	15.9 ± 8.1	...
Freq (GHz) (1)	(2)	Core (3)	C6 (4)	C5 (5)	C4 (6)	C3 (7)	C2 (8)	C1 (9)
4.634	P (mJy)	0.90 ± 0.55	1.06 ± 0.54	4.89 ± 0.46	1.46 ± 0.43	1.64 ± 0.43	3.82 ± 0.43	5.72 ± 0.43
	χ ($^\circ$)	97.1 ± 17.3	122.1 ± 14.5	89.4 ± 2.6	51.5 ± 8.5	15.0 ± 7.4	77.3 ± 3.2	28.8 ± 2.1
	m (%)	0.4 ± 0.2	0.4 ± 0.2	3.8 ± 0.3	1.6 ± 0.5	2.8 ± 0.8	5.4 ± 0.6	10.0 ± 0.7
4.754	P (mJy)	0.90 ± 0.54	0.83 ± 0.52	5.41 ± 0.44	1.75 ± 0.42	1.08 ± 0.41	3.76 ± 0.41	6.23 ± 0.41
	χ ($^\circ$)	50.9 ± 17.1	92.6 ± 18.0	75.7 ± 2.3	44.1 ± 6.8	11.2 ± 10.8	75.5 ± 3.1	26.8 ± 1.8
	m (%)	0.4 ± 0.2	0.4 ± 0.2	4.4 ± 0.3	1.8 ± 0.5	1.9 ± 0.7	5.6 ± 0.6	11.5 ± 0.7
4.974	P (mJy)	0.60 ± 0.52	2.21 ± 0.49	5.70 ± 0.40	1.39 ± 0.38	1.32 ± 0.37	2.94 ± 0.38	5.18 ± 0.37
	χ ($^\circ$)	38.0 ± 24.6	65.7 ± 6.3	68.9 ± 2.0	42.1 ± 7.8	21.4 ± 8.0	74.8 ± 3.6	25.7 ± 2.0
	m (%)	0.3 ± 0.2	0.9 ± 0.2	5.0 ± 0.3	1.7 ± 0.5	2.5 ± 0.6	4.5 ± 0.5	10.0 ± 0.7
5.055	P (mJy)	1.53 ± 0.52	2.20 ± 0.49	5.46 ± 0.40	1.05 ± 0.38	1.18 ± 0.38	2.88 ± 0.38	4.94 ± 0.38
	χ ($^\circ$)	2.2 ± 9.7	40.7 ± 6.4	58.8 ± 2.1	30.2 ± 10.4	10.1 ± 9.1	70.4 ± 3.7	23.8 ± 2.1
	m (%)	0.6 ± 0.2	0.9 ± 0.2	4.9 ± 0.3	1.9 ± 0.5	2.2 ± 0.6	4.4 ± 0.5	9.5 ± 0.7
Freq (GHz) (1)	(2)	Core (3)	X6 (4)	X5 (5)	X4 (6)	X3 (7)	X2 (8)	X1 (9)
8.120	P (mJy)	1.46 ± 0.56	3.03 ± 0.40	7.17 ± 0.37	1.42 ± 0.36	0.83 ± 0.36	0.68 ± 0.36	1.53 ± 0.36
	χ ($^\circ$)	72.4 ± 10.9	-55.6 ± 3.7	-1.0 ± 1.4	71.4 ± 7.2	58.4 ± 12.2	-71.8 ± 15.1	54.7 ± 6.6
	m (%)	0.5 ± 0.2	2.4 ± 0.3	9.7 ± 0.5	4.3 ± 1.1	4.2 ± 1.7	1.7 ± 0.8	8.5 ± 2.3
8.200	P (mJy)	1.55 ± 0.54	3.56 ± 0.38	6.80 ± 0.35	1.68 ± 0.34	0.90 ± 0.33	0.65 ± 0.34	1.09 ± 0.33
	χ ($^\circ$)	65.1 ± 10.0	-59.8 ± 3.0	-3.1 ± 1.4	69.8 ± 5.7	73.7 ± 10.6	-74.9 ± 14.8	54.5 ± 8.7
	m (%)	0.5 ± 0.2	2.9 ± 0.3	9.2 ± 0.5	5.2 ± 1.0	4.7 ± 1.7	1.7 ± 0.8	6.4 ± 2.2
8.400	P (mJy)	2.05 ± 0.53	2.46 ± 0.36	6.40 ± 0.33	1.24 ± 0.31	0.49 ± 0.31	0.74 ± 0.32	1.42 ± 0.31
	χ ($^\circ$)	60.0 ± 7.4	-66.1 ± 4.1	-5.6 ± 1.4	69.2 ± 7.2	73.4 ± 18.1	-75.2 ± 12.2	54.2 ± 6.2
	m (%)	0.7 ± 0.2	2.0 ± 0.3	8.6 ± 0.4	3.9 ± 0.9	2.7 ± 1.7	2.0 ± 0.8	8.9 ± 1.9
8.541	P (mJy)	1.73 ± 0.54	2.43 ± 0.37	6.78 ± 0.34	1.58 ± 0.33	0.69 ± 0.33	0.44 ± 0.33	1.17 ± 0.33
	χ ($^\circ$)	55.4 ± 8.9	-71.6 ± 4.3	-7.6 ± 1.4	67.5 ± 5.9	52.0 ± 13.5	-73.2 ± 21.4	53.3 ± 8.0
	m (%)	0.6 ± 0.2	2.0 ± 0.3	9.3 ± 0.5	5.1 ± 1.0	3.8 ± 1.7	1.3 ± 0.9	7.8 ± 2.0
Freq (GHz) (1)	(2)	Core (3)	U7 (4)	U6 (5)	U5 (6)	U4 (7)	U3 (8)	(9)
15.144	P (mJy)	3.13 ± 0.78	0.95 ± 0.74	0.22 ± 0.74	3.98 ± 0.74	1.91 ± 0.74	1.10 ± 0.74	...
	χ ($^\circ$)	74.5 ± 7.1	70.8 ± 22.3	93.8 ± 21.7	57.6 ± 5.3	141.5 ± 11.0	122.7 ± 19.2	...
	m (%)	1.8 ± 0.4	2.5 ± 1.9	0.6 ± 2.1	17.3 ± 3.2	12.7 ± 5.2	13.7 ± 9.2	...
15.224	P (mJy)	3.15 ± 0.82	1.52 ± 0.78	0.13 ± 0.78	3.37 ± 0.78	1.55 ± 0.78	1.24 ± 0.78	...
	χ ($^\circ$)	92.8 ± 7.4	75.7 ± 14.6	63.8 ± 22.3	43.6 ± 6.6	145.0 ± 14.3	135.8 ± 17.9	...
	m (%)	1.3 ± 0.4	4.0 ± 2.0	0.4 ± 2.1	14.0 ± 3.2	11.9 ± 5.9	17.7 ± 11.0	...
15.425	P (mJy)	3.38 ± 1.01	1.07 ± 0.98	0.30 ± 0.98	4.32 ± 0.98	1.03 ± 0.98	1.55 ± 0.98	...
	χ ($^\circ$)	95.1 ± 8.5	63.1 ± 14.6	75.7 ± 18.9	19.9 ± 6.5	12.9 ± 21.7	132.0 ± 18.0	...
	m (%)	1.9 ± 0.5	3.0 ± 2.8	0.9 ± 2.8	19.8 ± 4.2	8.0 ± 7.5	17.2 ± 10.8	...
15.565	P (mJy)	3.58 ± 1.15	1.17 ± 1.12	0.54 ± 1.12	4.17 ± 1.12	0.49 ± 1.12	1.37 ± 1.12	...
	χ ($^\circ$)	78.6 ± 9.2	75.2 ± 16.0	69.8 ± 19.4	20.4 ± 7.7	83.6 ± 20.0	117.3 ± 23.4	...
	m (%)	2.0 ± 0.6	3.3 ± 3.1	1.5 ± 3.2	16.7 ± 4.4	4.1 ± 9.3	17.2 ± 14.0	...

Notes: (1): Observing frequency. (2): Observed polarisation information of every components, including polarised flux density, polarised position angle and ratio of polarised flux to total flux of components. (3)-(9): Component ID from core to jet, consistent with the results from modelfitting.

Table 4. Parameters in the depolarization analysis.

Component (1)	$\ln m_0$ (%) (2)	RM (rad m ⁻²) (3)	b ($\times 10^5$ m ⁻⁴) (4)	R (5)
C6	-2.4 ± 0.4	1972 ± 207	-1.9 ± 0.3	-0.95
C5	-2.4 ± 0.1	722 ± 132	-0.5 ± 0.1	-0.96
C4	-3.7 ± 0.1	455 ± 96	-0.2 ± 0.1	-0.70
C3	-4.0 ± 0.4	...	0.2 ± 0.3	0.27
C2	-3.7 ± 0.1	152 ± 43	0.5 ± 0.1	0.91
C1	-2.5 ± 0.2	113 ± 36	0.2 ± 0.1	0.47
X6	-5.3 ± 0.5	2102 ± 124	8.8 ± 3.1	0.77
X5	-2.7 ± 0.2	780 ± 105	1.6 ± 1.3	0.50
X4	-2.9 ± 0.6	470 ± 127	-0.8 ± 0.3	-0.59
X3	-4.7 ± 0.9	...	8.5 ± 5.2	0.50
X2	-5.0 ± 0.8	3 ± 235	5.0 ± 4.6	0.43
X1	-2.2 ± 0.6	176 ± 138	-1.9 ± 1.8	-0.20

(1): Components name. (2): $\ln m_0$ in %. (3): Rotation Measure in rad m⁻². (4): the slope b in linear fitting. (5): Pearson correlation coefficient for linear fitting.**Table 5.** Spectral fit for the SSA and FFA models.

Model (1)	S_0 (Jy) (2)	τ (3)	α (4)	χ^2 (5)
SSA	0.25 ± 0.04	13.8 ± 2.9 (τ_s)	0.65	2.32
FFA	1.63 ± 0.5	1.1 ± 0.4 (τ_f)	0.65	2.53

(1): Absorbtion model. (2): S_0 in Jy. (3): Absorbtion coefficient. (4): the spectral index. (5) χ^2 for absorbtion fitting.

nearly $H\beta$ line, Hirst et al. (2003) found a very broad line width ~ 2200 km s⁻¹ in [OIII]₅₀₀₇ line. Using the [OIII]₅₀₀₇ line width as surrogate for the stellar velocity dispersion σ of the host galaxy $\sigma \sim \text{FWHM}([\text{OIII}]_{5007}/2.35)$, Nelson 2000), the broad [OIII]₅₀₀₇ line makes OQ172 different from the $M_{BH} - \sigma$ relation of local nearby galaxies (e.g., Tremaine et al. 2000)

$$M_{BH} = 10^{8.13} \left[\frac{\sigma}{200 \text{ km s}^{-1}} \right]^{4.02} M_{\odot}, \quad (8)$$

The large O[III]₅₀₀₇ line width could be due to the interaction between the jet and NLR. This is supported by the recent study of near-infrared spectra for a sample of powerful young radio quasars by Kim et al. (2013), who found their [OIII]₅₀₀₇ lines are exceptionally broad, with FWHM $1300 \sim 2100$ km s⁻¹, significantly larger than those of ordinary distant quasars. They argued that these large line widths could be explained by jet-induced outflows, as predicted by theoretical models of AGN feedback.

All the available data that the jet bending and violent RM variations occur at about 3 mas from the core. The Faraday depolarisation appears to be caused by the internal medium in the jet itself. The radio emission of the core region demonstrates a spectrum with the turnover. Together with the broad O[III]₅₀₀₇ line, all these properties are closely related and likely caused by the same nuclei medium, presumably in the NLR.

4 CONCLUSIONS

We presented a VLBA polarimetry observation of the high-redshift GPS quasar OQ172 at five frequency bands. Our conclusions are as follows:

- A core-jet morphology has been found at all five frequencies with sharp bending at ~ 3 mas from the core clearly visible at 4.8, 8.3, and 15.3 GHz.
- Linearly polarised emission has been detected in OQ172 at all five frequencies, with a typical low fractional polarisation in the core, and high in the jet components. The rotation measure obtained at 4.8 and 8.3 GHz, shows the highest values of ~ 2000 rad m⁻² in the innermost region, dropping down to ~ 700 rad m⁻² at 3 mas, and decreasing to lower values toward the outer jet regions.
- The simultaneous multi-frequency observation enables us to consider the turnover spectra within the framework of SSA and FFA absorption models. While a specific model of absorption cannot be determined yet, some conclusions on physical parameters in the core region can be made.
- A combination of the presented here and discussed observing properties of the high-redshift GPS quasar OQ172 (the bending structure of its VLBI jet, spectral turnover of compact components and the broad O[III]₅₀₀₇) indicates on a possible role of the same physical medium in the NLR.

ACKNOWLEDGMENTS

We thank the anonymous referee for insightful comments and constructive suggestions. We are grateful to A.B. Fletcher for helpful discussions and proofreading of the observing proposal. This work is supported by the National Natural Science Foundation of China (Grant No. 11233006, 11473069, 11273042, U1231106 and U1431111). YL also acknowledges support from the Grant BK20131460. MFG acknowledges support from the National Science Foundation of China (grants 11473054 and U1531245) and by the Science and Technology Commission of the Shanghai Municipality (14ZR1447100). The VLBA is operated by the Na-

tional Radio Astronomy Observatory which is managed by Associated Universities, Inc., under cooperative agreement with the National Science Foundation. The National Radio Astronomy Observatory is a facility of the National Science Foundation operated under cooperative agreement by Associated Universities, Inc. This paper has made use of the NASA/IPAC Extragalactic Database (NED), which is operated by the Jet Propulsion Laboratory, California Institute of Technology, under contract with the National Aeronautics and Space Administration.

REFERENCES

- Bicknell, G.V., Dopita, M.A., & O’Dea, C.P., 1997, ApJ 485: 112
- Blandford R. D., Königl A., 1979, ApJ, 232, 34
- Burn, B. J., 1966, MNRAS, 133, 67
- Chen, Y. J., Shen, Z. Q. Feng, S. W., 2010, MNRAS, 408, 841
- Chen, Y. J., Zhao, G. Y., Shen, Z. Q., 2011, MNRAS, 416, 109
- Dallacasa, D., Fanti, C., Fanti, R., Schilizzi, R.T., & Spencer, R.E., 1995, A&A 295: 27
- Edwards, P. G., Tingay, S. J., 2004, A&A, 424, 91
- Fey, A.L., & Charlot, P., 2000, ApJS 128: 17
- Fomalont, E.B., Frey, S., Paragi, Z., Gurvits, L.I., Scott, W.K., Taylor, A.R., Edwards, P.G., & Hirabayashi, H., 2000, ApJS 131: 95
- Gallimore, J. F., Elitzur, M., Baum, S. A., 2006, LNP, 693, 101
- Ghisellini, G., Padovani, P., Celotti, A., Maraschi, L., 1993, ApJ, 407, 65
- Greene, J. E. & Ho, L. C. 2005, ApJ, 630, 122
- Gu, M. F., Chen, Z. Y., & Cao, X. W. 2009, MNRAS, 397, 1705
- Gurvits L.I. 2003, In Active Galactic Nuclei, ASP Conf Series vol. 290, p. 51
- Hirst, P., Jackson, N., & Rawlings, S., 2003, MNRAS 346: 1009
- Homan, D., C., Ojha, R., Wardle, J. F. C., et al. 2002, ApJ, 568, 99
- Homan, d .C., Lister, M. L., Aller, H. D., Aller, M. F., Wardle, F. C., 2009, ApJ, 696, 328
- Hovatta, T., Lister, M. L., Aller, M. F., Aller, H. D., Homan, D. C., Kovalev, Y. Y., Pushkarev, A. B., Savolainen, T., 2012, AJ, 144, 105
- Kameno, S., Horiuchi, S., Shen, Z. Q., Inoue, M., Kobayashi, H., Hirabayashi, H., Murata, Y. 2000, PASJ, 52, 209
- Kong M.-Z., Wu X.-B., Wang R., & Han, J.-L. 2006, ChJAA, 6, 396
- Königl A., 1981, ApJ, 243, 700
- Kormendy J., Richstone D., 1995, ARA&A, 33, 581
- Liu, Y., & Jiang, D. R., 2006, ChA&A, 6, 655
- Liu, Y., Jiang, D. R., Gu, M. F., 2013, IAUS, 290, 271
- Liu, Y., Jiang, D. R., Gu, M., Gurvits, L. I., 2016, AN, 337, 101
- Magorrian J. et al., 1998, AJ, 115, 2285
- Mantovani, F., Junor, W., Bondi, M., Cotton, W., Fanti, R., Padrielli, L., Nicolson, G.D., & Salerno, E., 1998, A&A 332: 10
- Mantovani, F., Mack, K.-H., Montenegro-Montes, F. M., Rossetti, A., & Kraus, A., 2009, A&A, 502, 61
- Nelson, C. H., 2000, ApJL, 544, 91
- O’Dea, C.P., Baum S.A., & Stanghellini C., 1991, ApJ 380: 66
- O’Dea, C.P., & Baum S.A., 1997, AJ 113: 148
- O’Dea, C.P., 1998, PASP 110: 493
- Oppermann, N., Junklewitz, H., Robbers, G., et al. 2012, A&A, 542, 93
- Peterson, B. M., 1997, iagn, book, P
- Pshirkov, M. S., Tinyakov, P. G., Kronberg, P. P., Newton-McGee, K. J., 2011, 738, 192
- Punsly, B., 2005, ApJL, 623, 9
- Punsly, B., 2007, ApJL, 374, 10
- Pushkarev, A. B., 2001, Astron. Rep., 45(9), 667
- Readhead A.C.S., 1994, ApJ, 426, 51
- Rossetti, A., Dallacasa, D., Fanti, C., Fanti, R., & Mack, K.-H., 2008, A&A, 487, 865
- Snellen, I. A. G., Schilizzi, R.T., Miley, G.K., de Bruyn, A.G., Bremer, M.N., & Röttgering, H.J.A., 2000, MNRAS 319: 445
- Spencer, R. E., McDowell, J. C., Charlesworth, M., Fanti, C., Parma, P., & Peacock, J. A., 1989, MNRAS, 240, 657
- Spitzer, L. 1978, Physical Processes in the Interstellar Medium (New York: Wiley)
- Stanghellini, C., O’Dea, C. P., Dallacasa, D., Baum, S. A., Fanti, R., Fanti, C., 1998, A&AS, 131, 303
- Steppe, H., Jeyakumar, S., Saikia, D. J., Salter, C. J., 1995, A&AS, 113, 409
- Taylor, G. B., Inoue, M., & Tabara, H., 1992, A&A, 264, 421
- Taylor G.B., 1998, ApJ, 506, 637
- Tremaine S. et al., 2002, ApJ, 574, 740
- Tribble, P. C., 1991, MNRAS, 250, 726
- Xie, G. Y., Jiang, D. R. & Shen, Z. Q., 2005, ApJL, 621, 13
- Udomprasert, P.S., Taylor, G.B., Pearson, T.J., & Roberts, D.H., 1997, ApJL 483, 9
- Urry, C. M. & Padovani, P., 1995, PASP, 107, 803
- Zavala, R. T. & Taylor, G. B., 2004, ApJ, 612, 749

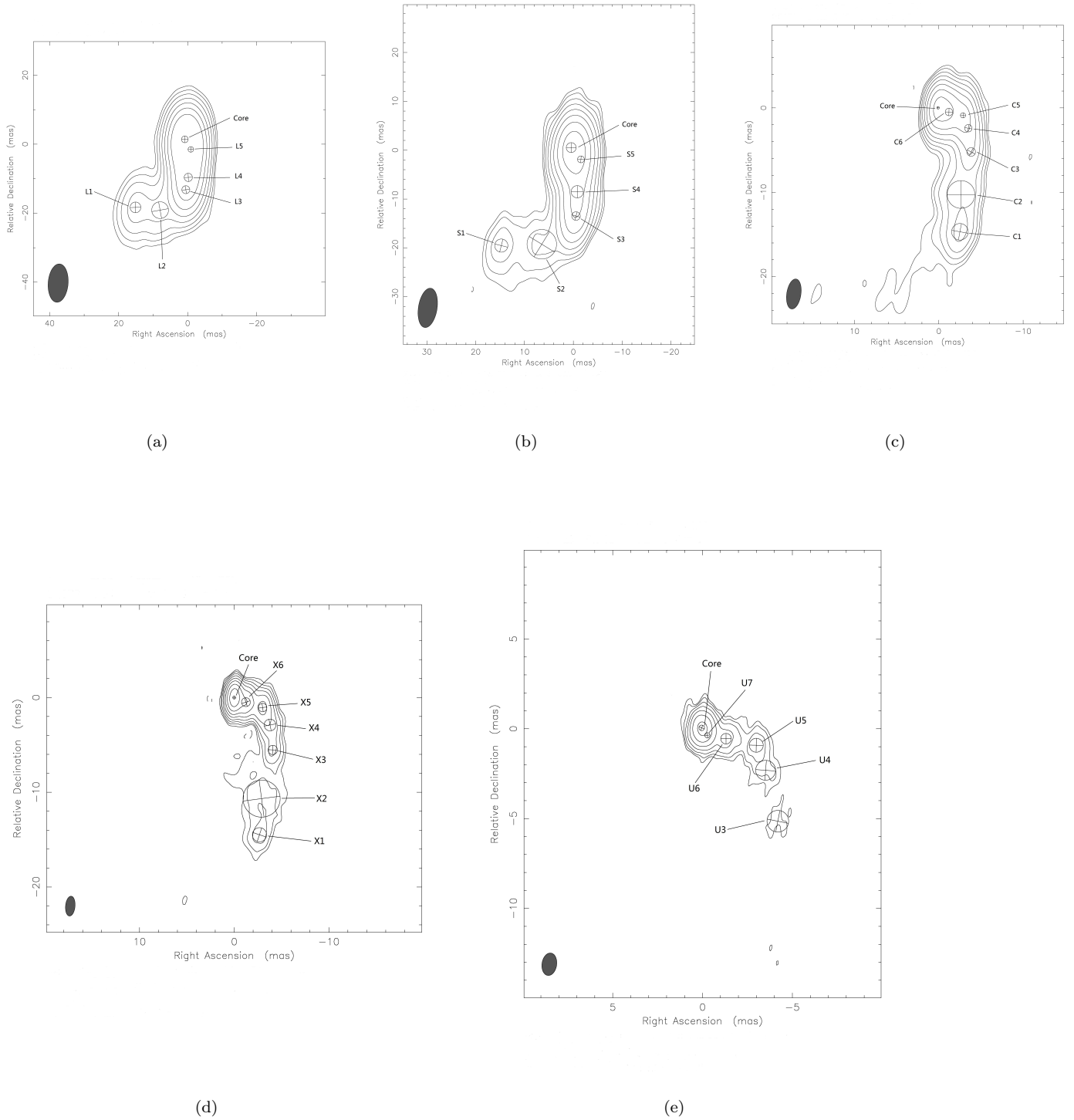


Figure 1. Model fit to the total intensity visibilities at 1.6 GHz (a), 2.2 GHz (b), 4.8 GHz (c), 8.3 GHz (d) and 15.3 GHz (e) for the GPS quasar OQ172. The peaks and beams are the same as Fig.2 - Fig.6 in Liu et al. (2016) for all five frequencies. Each component is represented by an elliptic form with the fitted position, size and orientation (see details in Table 2.).

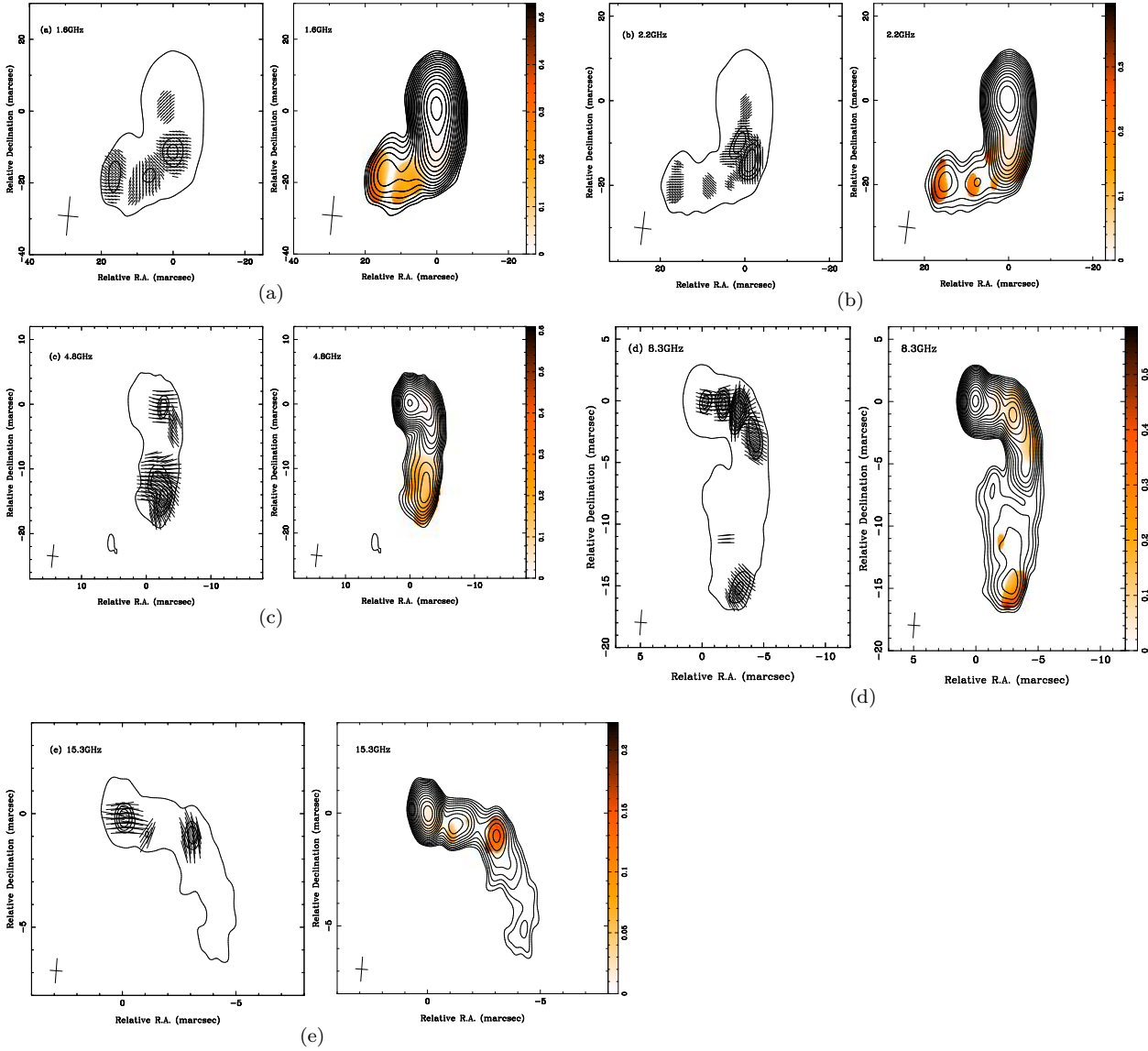


Figure 2. Polarisation distribution images for the observation of GPS quasar OQ172 at five frequency bands. The left image in each panel is an EVPA distribution (solid line) with contours of continuum intensity overlaid; the right shows the polarised intensity (color) overlaid by total intensity contours. The lowest contours for total and linearly polarised intensity distributions are 3 times the noise level. The color wedge at each right image shows the fractional polarisation. (a): The restoring beam has dimensions of $11.2 \text{ mas} \times 5.81 \text{ mas}$ at position angle -4.47° , indicated at the bottom left corner. Contours start at $4.21 \text{ mJy beam}^{-1}$ and increase by factors of 2. (b): The restoring beam has dimensions of $8.15 \text{ mas} \times 3.15 \text{ mas}$ at position angle -9.10° , indicated at the bottom left corner. Contours start at $3.91 \text{ mJy beam}^{-1}$ and increase by factors of 2. (c): The restoring beam has dimensions of $3.6 \text{ mas} \times 1.69 \text{ mas}$ at position angle -8.79° , indicated at the bottom left corner. Contours start at $1.64 \text{ mJy beam}^{-1}$ and increase by factors of 2. (d): The restoring beam has dimensions of $2.1 \text{ mas} \times 1.0 \text{ mas}$ at position angle -5.25° , indicated at the bottom left corner. Contours start at $1.30 \text{ mJy beam}^{-1}$ and increase by factors of 2. (e): The restoring beam has dimensions of $1.26 \text{ mas} \times 0.82 \text{ mas}$ at position angle -8.31° , indicated at the bottom left corner. Contours start at $2.25 \text{ mJy beam}^{-1}$

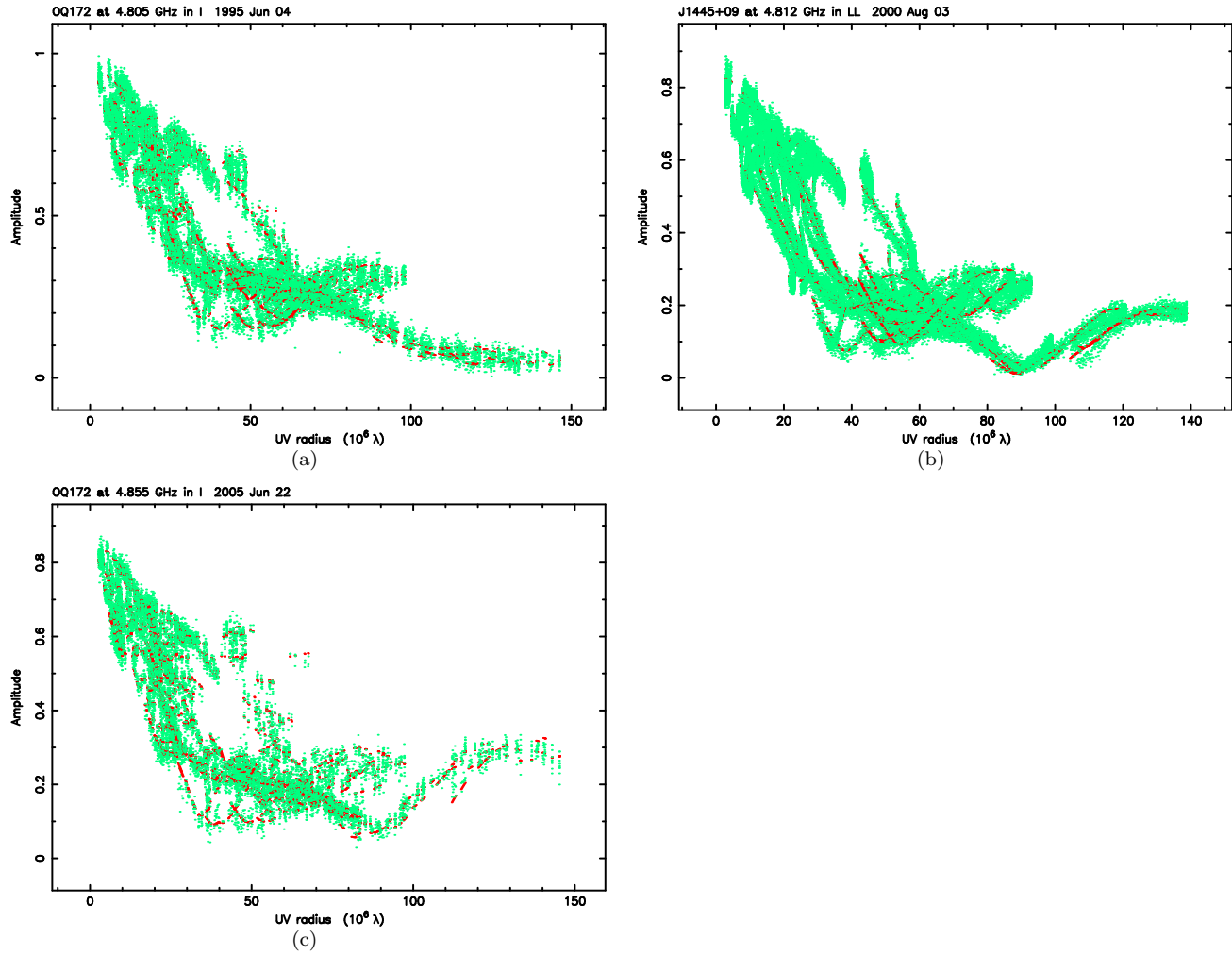


Figure 3. (a): The visibility amplitude for OQ172 observed at 5.0 GHz with VLBA on 1995.4 (Udomprasert’s data, VLBA project code BT010); (b): The visibility amplitude for OQ172 observed at 5.0 GHz with VLBA on 2000.6 (VLBA project code W035); (c): The visibility amplitude for OQ172 observed at 4.8 GHz with VLBA on 2005.5 (our data in this work, VLBA project code BL129).

Rotation Measures in Core in OQ172

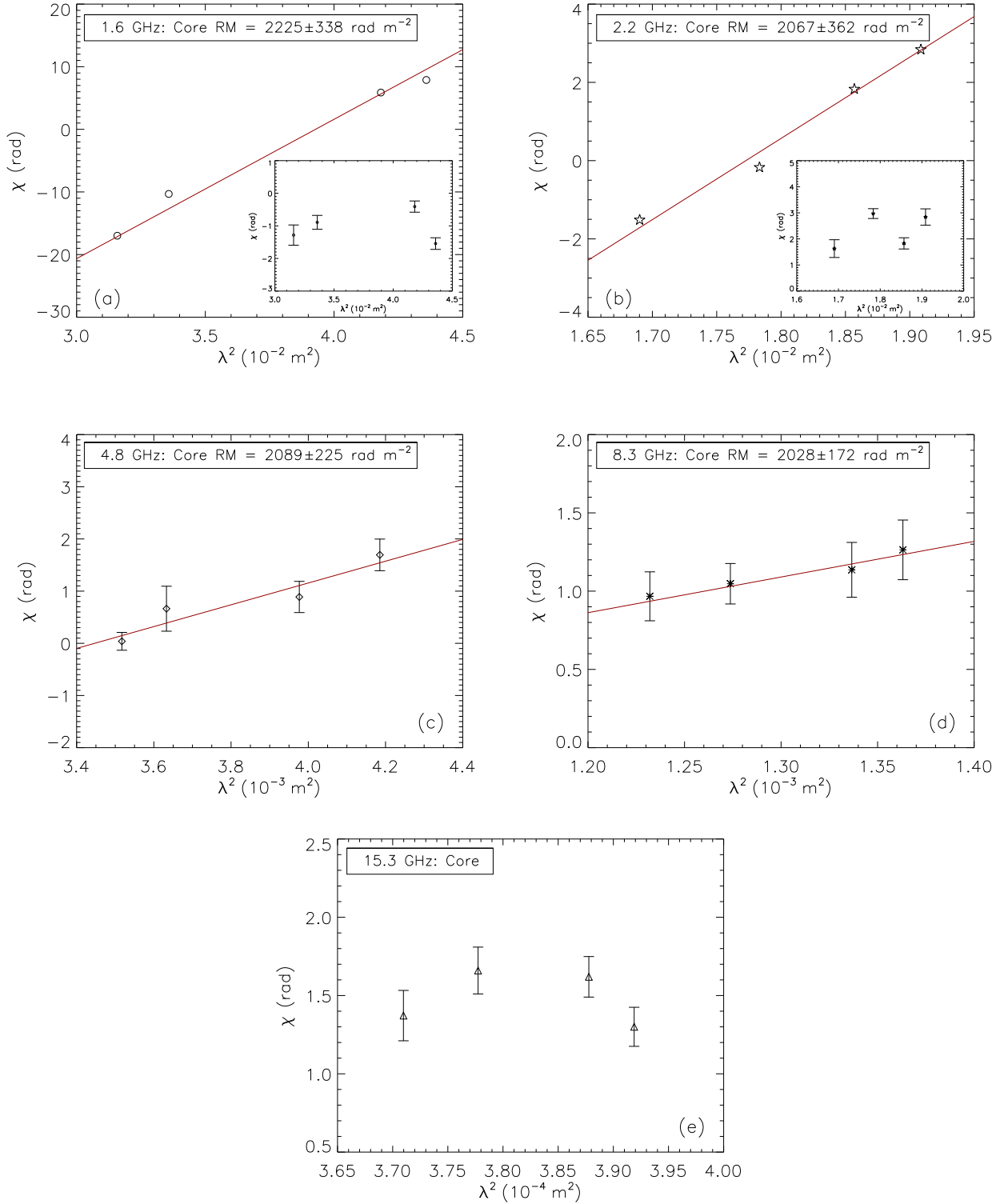


Figure 4. Rotation Measure for the quasar OQ172 in the core component at five frequencies. The different kind of symbols are represented different frequencies: circles for 1.6 GHz, pentagrams for 2.2 GHz, diamonds for 4.8 GHz, stars for 8.3 GHz, and triangles for 15.3 GHz, respectively.

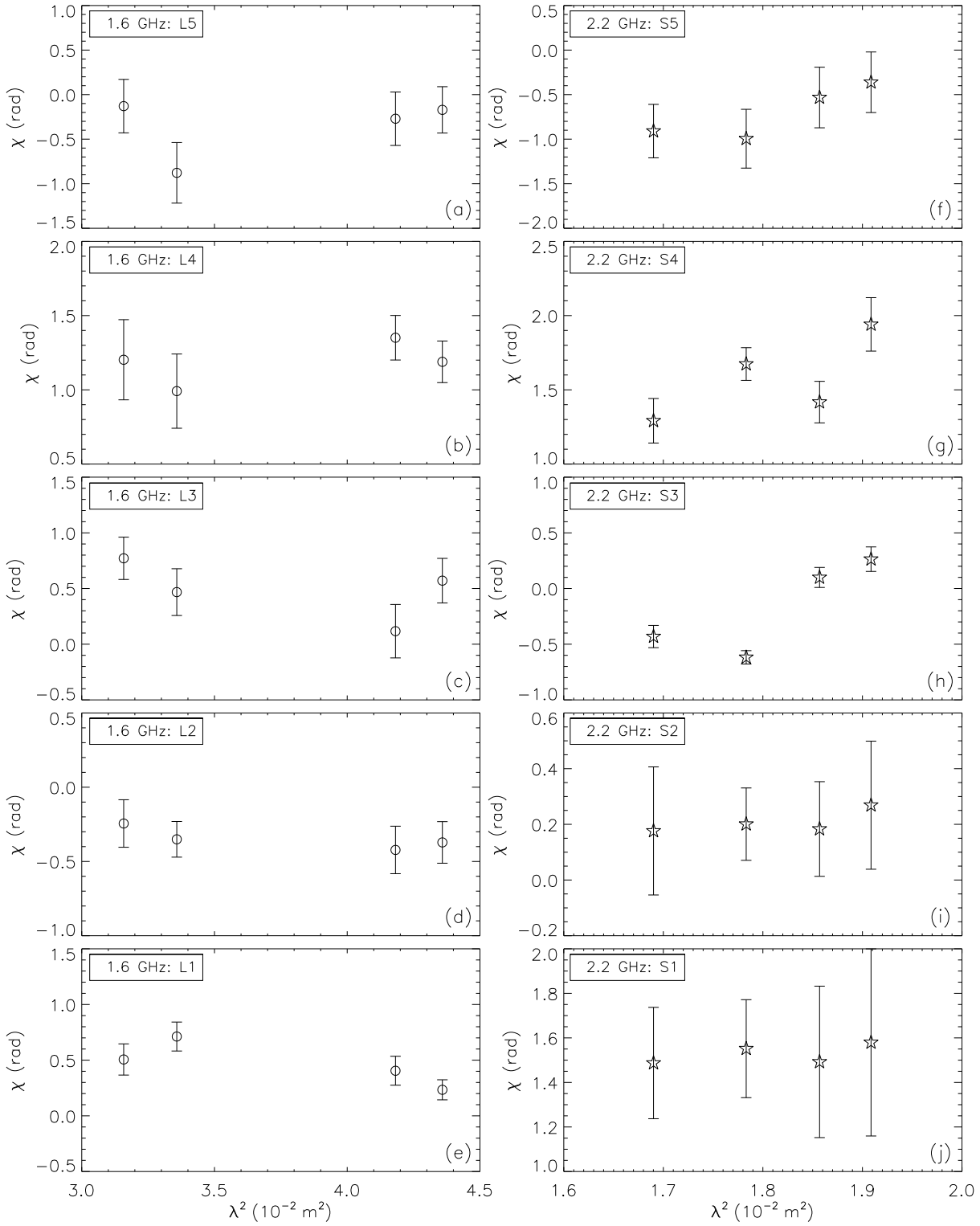


Figure 5. Rotation Measure for the quasar OQ172 in the jet components at 1.6 and 2.2 GHz. The circles show the components at 1.6 GHz and the pentagrams display that at 2.2 GHz.

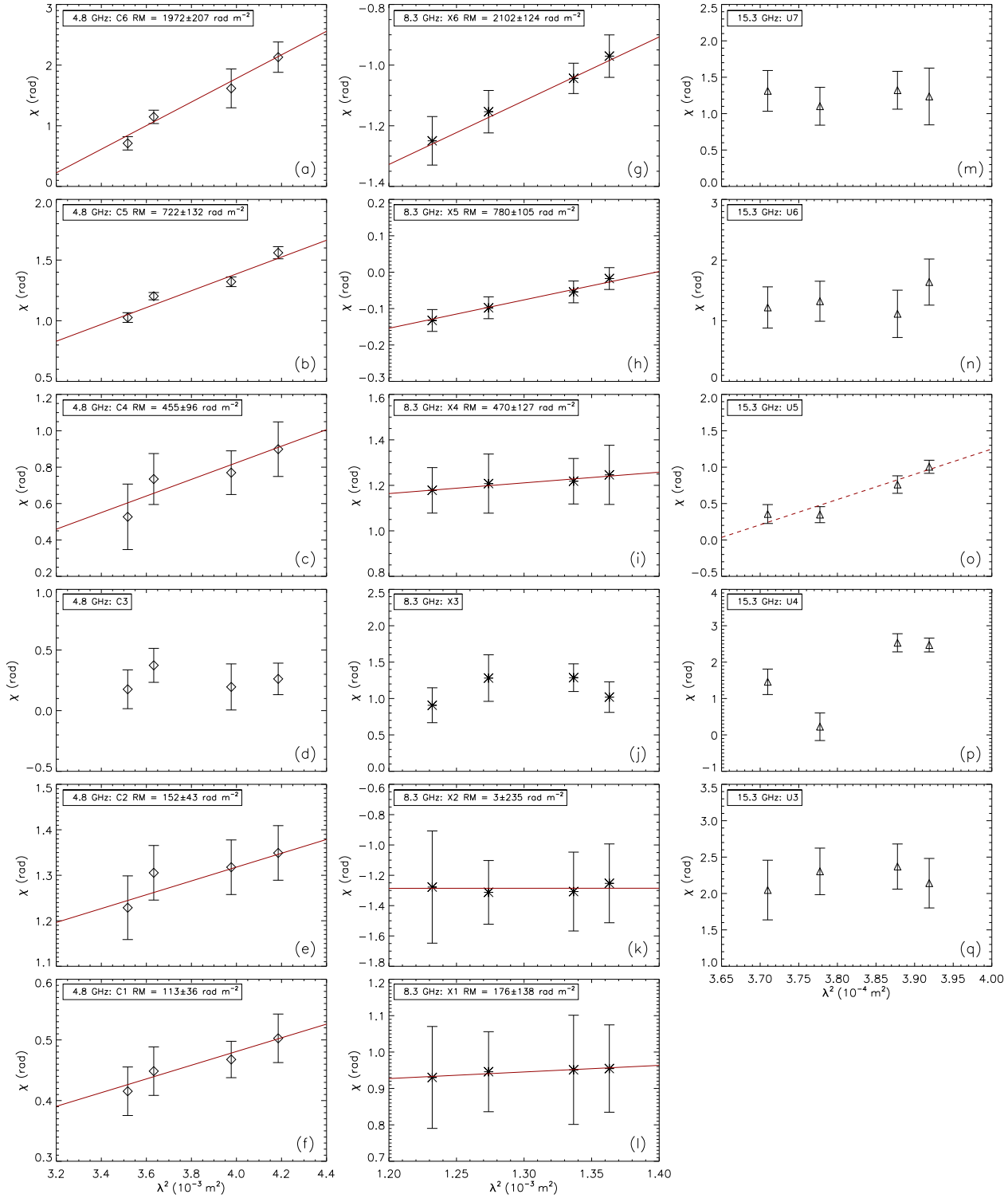


Figure 6. Rotation Measure for the quasar OQ172 in the jet components at 4.8, 8.3 and 15.3 GHz. The diamonds present the components at 4.8 GHz, the stars describe the components at 8.3 GHz, and the triangles indicate the components at 15.3 GHz, respectively.

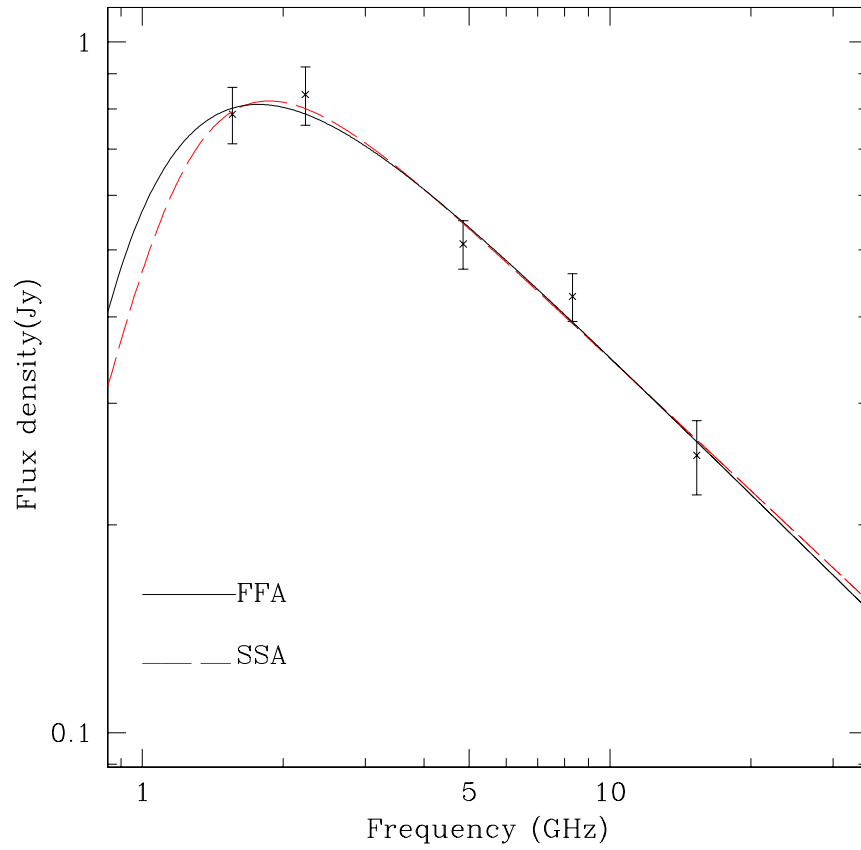


Figure 7. The core region component five-frequency spectrum from our VLBA observation. The points with the error bars show the flux density of the core region component, and the black line and red dashed line indicate the fitted spectra for FFA and SSA models, respectively.